IAES International Journal of Robotics and Automation (IJRA)
Vol. 15, No. 4, December 2026, pp. 902~912
ISSN: 2722-2586, DOI: 10.11591/ijra.v15i4.pp 902-912

Design, analysis, and implementation of ZER0: A low-cost, modular autonomous mobile robot vacuum cleaner using additive manufacturing and SLAM

Eman Ebrahim, Ibrahim Al Souleiman
Swiss International University, Zurich, Switzerland

Article Info

Article history:

Received Dec 2, 2025
Revised Aug 29, 2026
Accepted Nov 10, 2026

Keywords:

Backward-curved blades
Centrifugal impeller
LiDAR
Mechatronics
Robotic vacuum cleaner
SLAM

ABSTRACT

This paper presents the comprehensive design, analysis, and implementation of "ZER0," an autonomous mobile robot vacuum cleaner developed as a unified, reproducible mechatronic platform. The system integrates optimized structural geometry, advanced fluid dynamics, and intelligent navigation through the convergence of additive manufacturing, computational simulation, and embedded control systems. A hybrid chassis combining a semicircular front for obstacle deflection and a reinforced rectangular rear for component stability is fabricated using Fused Deposition Modeling (FDM) with PLA+ material. The centrifugal suction system, driven by a high-speed 775-series DC motor and featuring backward-curved impeller blades, achieves a measured static pressure rise of 198 Pa (±12 Pa) with 47% fan efficiency, closely matching CFD predictions. Structural integrity is validated via Finite Element Analysis (FEA) and physical testing, yielding a Factor of Safety of 11.8 for general loads and 4.8 for impact scenarios. Comprehensive experimental validation confirms thermal stability (<65 °C), navigation accuracy (RMSE = 0.042 m), and coverage efficiency (97.3%). Autonomous navigation is achieved through a LiDAR-based SLAM pipeline on a Raspberry Pi 4, utilising ROS 2 with slam_toolbox and Nav2. A controlled experimental methodology, including a random-walk control group and statistical hypothesis testing, demonstrates that the systematic Boustrophedon coverage strategy significantly outperforms stochastic methods ($p < 0.001$). The total system cost of approximately 24,032 EGP (~308 USD) demonstrates the feasibility of high-performance autonomous robotics outside proprietary industrial ecosystems. The project establishes a scalable, open-source blueprint for cost-effective domestic automation and robotics education through the strategic integration of mechanical engineering, fluid mechanics, and artificial intelligence.

This is an open access article under the CC BY-SA license.

Corresponding Author:

Eman Ebrahim
Swiss International University (SIU)
Switzerland, Zurich
Email: dr.n.eman@swiss.edu.eu

1. INTRODUCTION

Robotic vacuums have evolved from random-walk to SLAM-based systems, yet a critical accessibility gap persists commercial platforms (Roomba, Roborock, Ecovacs) are costly, proprietary, and non-repairable [1], [2], while opensource kits (TurtleBot, Create 3) lack integrated vacuuming, aerodynamic optimisation, and structural workflows for suction ducts [1]. Additive manufacturing Fused Deposition Modeling (FDM) has been used for robotic components, but systematic validation of printed impellers and

volutes is limited due to anisotropy and surface roughness [3]. SLAM algorithms have matured (frontier exploration, Boustrophedon coverage, DWA) [4], [5], yet low-cost platforms rarely incorporate payload-specific dynamics (motor vibration, filter loading, mass distribution), leaving a gap in understanding their effect on localisation and path execution. ZER0 directly addresses this with four contributions: i) the first fully opensource robot vacuum integrating LiDAR SLAM, systematic coverage, and FDM manufacturing, with complete CAD, PCB, and software releases; ii) validated FDM-printed impeller performance (CFD error <6%); iii) statistical demonstration that Boustrophedon coverage significantly outperforms random-walk; and iv) a cost-performance advantage at ~¼ the price of comparable SLAM-equipped development platforms. Beyond hardware, ZER0 enables affordable, reproducible research and pedagogy in domestic automation, multiroom navigation, and human-robot interaction.

2. THE PROPOSED METHOD/ALGORITHM/PROCEDURE

2.1. Mechanical design and structural integrity

The structural geometry of an indoor robot is the primary determinant of its spatial efficiency and collision resilience. The ZER0 platform uses a hybrid chassis geometry designed to balance maneuverability with internal volume. The leading edge is a true semicircle, which minimizes the collision surface area and distributes impact loads along an arc. This geometry allows the roller brush to extend across the full width of the robot, maximizing the sweep-to-diameter ratio—a key metric for cleaning coverage. The rear section features a rectangular plan with large-radius fillets, allowing the robot to follow walls fleshly and access corners more effectively than fully circular designs. Internally, the flat planes provide stable mounting for the L298N driver, XL4016 regulators, and battery assembly. Figure 1 shows the physical 3D-printed chassis and the digital CAD model. Material Selection Rationale. PLA+ (eSUN PRO-PLA) was selected as the primary structural material based on its superior mechanical properties compared to standard PLA and ABS [6]. To justify this selection quantitatively, Table 1 summarizes the comparative mechanical performance of these candidate materials, with data derived from manufacturer technical datasheets and prior FDM characterization studies [3]. As shown in the table, PLA+ offers higher tensile strength than both standard PLA and ABS, combined with excellent impact resistance and very strong layer adhesion—properties that are critical for a mobile robot subject to repeated collisions and vibration.



Figure 1. Physical 3D-printed chassis showing "tree-like" support structures and internal mounting bosses (left) alongside the digital CAD model (right)

Table 1. Mechanical performance comparison of structural materials

Property	PLA+	PLA	ABS
Tensile Strength	~50 MPa	~37 MPa	~40 MPa
Impact Resistance	Excellent	Brittle	Good
Print Stability	High	Very High	Low (warping)
Layer Adhesion	Very Strong	Moderate	Weak-Moderate

Structural validation was performed via Finite Element Analysis (FEA) using ANSYS Mechanical 2023 R2 under worst-case loading conditions (Figure 2). Material properties were assigned as: Young's modulus E = 2,888 MPa, Poisson's ratio ν = 0.36, density ρ = 1,230 kg/m³. Loads included self-weight of internal components (total mass 1.2 kg) distributed over their mounting areas, and an impact force of 20 N applied at the front-arc region to simulate collision with furniture. Boundary conditions fixed the four-wheel mounting points in all degrees of freedom. The mesh consisted of tetrahedral quadratic elements with global size 2 mm and local refinement of 0.5 mm at stress concentration zones; a mesh convergence study confirmed that further refinement changed stress results by less than 2%. The analysis yielded a Factor of

Safety (FoS) of 11.8 for general internal loads (σmax, von Mises = 4.5 MPa);(FoS = 53/4.5 = 11.8) and 4.8 for front-arc impacts (σmax = 11.0 MPa) ; (FoS = 53/11.0 = 4.8). The maximum displacement was 0.31 mm at the cantilevered roller holder arm, remaining within the bearing-seat fit tolerance of ±0.4 mm, ensuring that the roller brush maintains rotational alignment without mechanical binding. While the theoretical mass of the body at 100% infill is approximately 4.9 kg, the implementation of 20–30% gyroid infill—a pattern chosen for its isotropic strength properties [3]—reduced the actual printed mass to a range of 900–1,200 g. This reduction is vital for maintaining the power-to-weight ratio necessary for efficient locomotion and extended battery life.

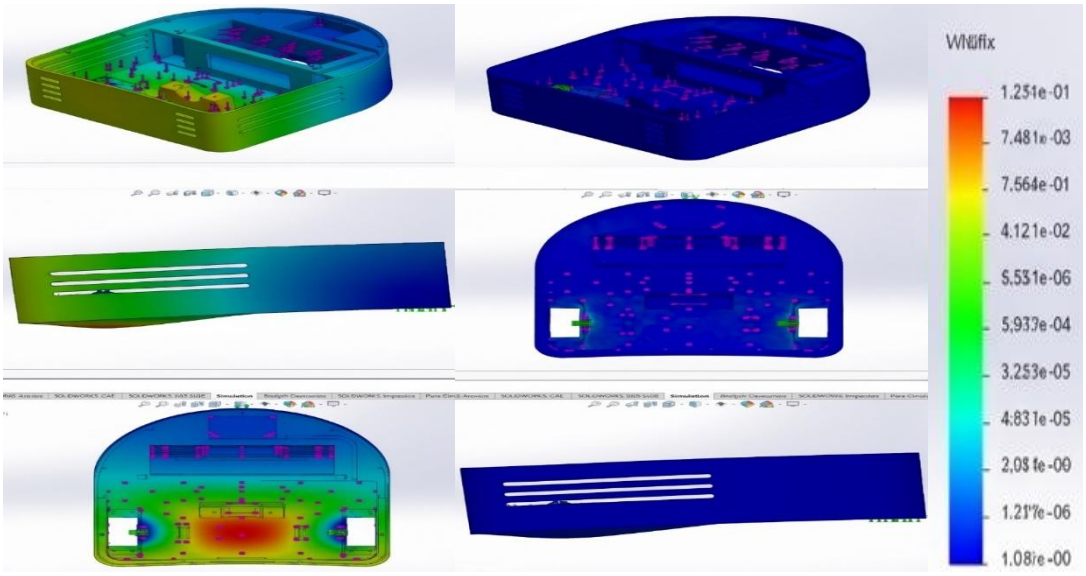

Figure 2. Multi-view body stress analysis validating load distribution and safety margins

2.2. Aerodynamic optimization and fluid dynamics

The ZER0 suction system uses a backward-curved centrifugal impeller (775-series motor) [7] with a self-limiting power curve to prevent current surges under rising flow resistance. Internal airflow follows: inlet → dust chamber → impeller → electronics cooling zone → rear exhaust. CFD analysis (k–ω SST, $y^+ \approx 1$, pressure inlet at 0 Pa, mass-flow outlet of 0.014 kg/s corresponding to 4.2 m/s inlet velocity) predicted a 210 Pa static pressure rise and a secondary forced-convection effect (~0.8 m/s) over motor drivers for passive thermal management. The Archimedean volute casing, sealed by a 0.1 mm interference tongue-and-groove joint, minimizes leakage. Table 2 compiles these key aerodynamic metrics, serving as benchmark targets for the experimental validation.

Table 2. Aerodynamic performance metrics

Parameter	Value	Significance
Static Pressure Rise	210 Pa	Overcomes filter resistance
Inlet Velocity	4.2 m/s	Efficient debris entrainment
Exhaust Velocity (Cooling)	~0.8 m/s	Passive thermal management
Fan Efficiency	~42%	Typical for FDM-printed centrifugal fan

The fan efficiency η was calculated from simulated power and flow data as:

$$\eta = \frac{\Delta P \cdot Q}{P_{\text{shaft}}}$$

with $P_{\text{air}} = 210\ \text{Pa} \times 0.012\ \text{m}^3/\text{s} = 2.52\ \text{W}$ and shaft power estimated from motor torque and speed, the predicted efficiency was 42%. This value is typical for FDM-printed centrifugal fans given surface roughness and tolerance constraints. The volute scroll ensures a gradual deceleration of the flow, minimizing losses.

Figure 3 shows the internal airflow path class diagram and the assembled impeller/volute components, while Figure 4 presents the impeller flow field visualization.

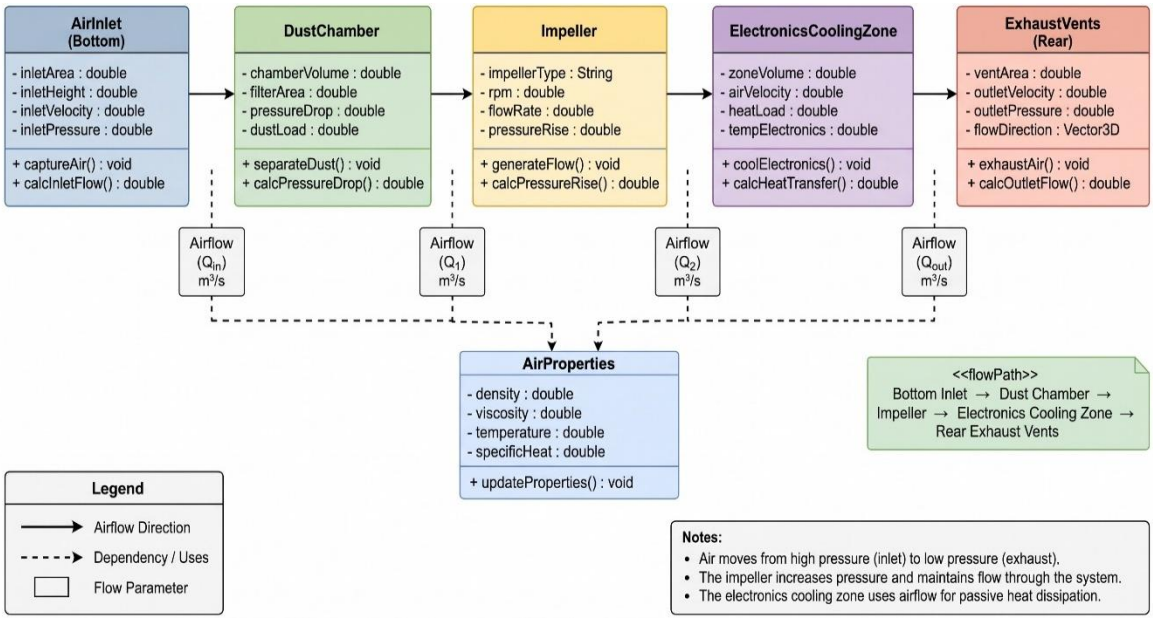

Figure 3. Internal airflow path class diagram and the assembled impeller/volute components

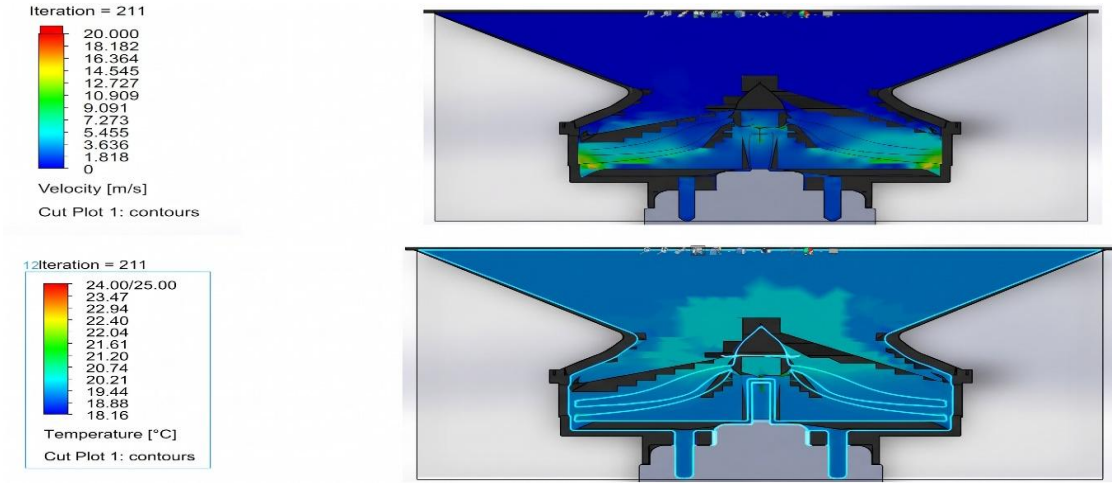

Figure 4. Impeller flow analysis

The aerodynamic design was treated as a coupled rotor–volute problem rather than as an isolated impeller optimization task. In particular, the backward-curved blade geometry was selected to reduce sensitivity to increasing system resistance, while the scroll profile was shaped to recover part of the dynamic pressure as static pressure. This approach is relevant to low-cost additive manufacturing because printed surface roughness and dimensional tolerances can otherwise produce appreciable secondary losses. The simulation therefore served not only to estimate peak pressure but also to identify a manufacturable operating point that could be reproduced experimentally.

2.3. Electronic architecture and power distribution

ZER0's modular hardware stack isolates power domains to mitigate EMI, separating high-current motor loads from the Raspberry Pi 4 logic plane (BCM2711, 4 GB RAM) [8]. Sensing is via an RP-LiDAR A1 (360°, 12 m range) [9]. Locomotion uses GA25-YN370 12 V/200 RPM motors driven by an L298N H-

bridge (2 A/channel, thermal protection) [10], while a 96%-efficient XL4016 buck converter (8 A limit) [11] supplies the stable 5 V rail. The hardware specifications are presented in Table 3.

Table 3. Key hardware specifications

Component	Specification	Function
Raspberry Pi 4B	BCM2711, 4GB RAM, 1.8 GHz	Main controller & ROS2 host
RPLiDAR A1	360° laser scanner, 12m range	Environmental mapping
GA25YN370 Motors	12V, 200 RPM, 4.5 kg·cm stall torque	Differential drive
L298N Driver	Dual H-Bridge, 2A/channel	Motor control
XL4016 Buck	8A, 96% efficiency, 180 kHz	5V power regulation

The custom PCB (KiCad 9, 100×80 mm, 2 oz power / 1 oz signal copper) centralizes power and motor control via a hierarchical topology: XL4016E buck converter → intermediate bus → dual LM7805 regulators [12] and drivers, plus an MCU-independent CC-CV charger (MCP602). Total input is 103.76 W (12 V, 8.65 A), with useful output of 80 W (72 W motor, 2.4 W logic, 1.6 W sensors, 4.0 W driver losses), yielding 77.1% efficiency. Losses distribute as: LM7805s (11.2 W), L298N (7.44 W), XL4016 (3.18 W), and parasitics (1.98 W); the IRLZ44N suction MOSFET achieves 97.2% efficiency (0.62 W loss, 22 W output). The design strictly separates high-current and logic domains to mitigate transients and noise that could affect LiDAR, processor, and sensor timing. This hierarchical approach offers a cost-effective, serviceable, and robust solution while enabling individual module upgrades without full architecture redesign.

2.4. Software logic, mapping, and navigation

Autonomy is implemented via a ROS 2–Arduino bridge [13], employing slam_toolbox for real-time mapping [14], [15] and Nav2 for planning [16]. Cleaning follows a Boustrophedon zigzag pattern generated by a Coverage Planner over segmented room grids, reducing redundancy versus stochastic methods. Active-SLAM with Frontier Detection identifies unknown-space boundaries to minimize map entropy [17], [18], ensuring accurate localization and obstacle avoidance [19], [20]. Figure 5 illustrates the pipeline from raw LiDAR scans through slam_toolbox mapping to Nav2 goal execution.

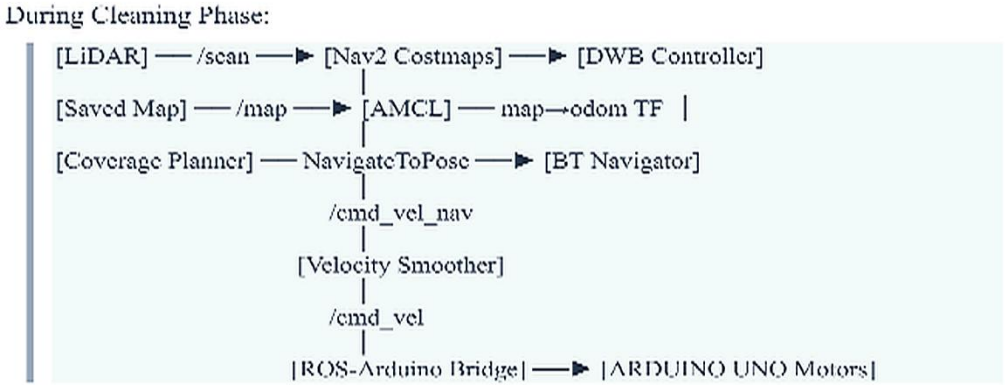

Figure 5. Autonomous active-SLAM exploration data flow pipeline, illustrating the sequence from raw LiDAR scans to slam_toolbox mapping and Nav2 goal execution

2.4.1. ROS-Arduino bridge and low-level control

The ROS–Arduino Bridge communicates via USB serial using an ASCII protocol: e returns encoder ticks, m sets target wheel speeds. Closed-loop PID velocity control runs on the Arduino at 100 Hz. Parameters tuned via Ziegler–Nichols (critical gain K_u, period P_u) are $K_p = 2.8$, $K_i = 0.9$, $K_d = 0.15$, yielding 0.6 s rise time, <3% steady-state error, and <8% overshoot. Integral anti-windup (±255) and a first-order derivative filter (0.7) are implemented for robustness.

2.4.2. Coverage planning algorithm

To ensure replicability, Algorithm 1 presents the pseudocode for the Boustrophedon Coverage Planner node. The algorithm decomposes the occupancy grid [21] into rectangular c ells, generates

alternating parallel paths within each cell, and publishes sequential `NavigateToPose` goals to the Nav2 Behavior Tree (BT) Navigator.

Algorithm 1: Boustrophedon Coverage Planner
Input: OccupancyGrid map, robot_footprint, stripe_width
Output: Sequence of goal poses G = [g_1, g_2, ..., g_n]
1: cells ← DecomposeGrid(map, robot_footprint)
2: G ← empty list
3: for each cell in cells do
4: stripes ← GenerateParallelStripes(cell, stripe_width)
5: direction ← 1 // 1 = left-to-right, -1 = right-to-left
6: for each stripe in stripes do
7: if direction == 1 then
8: start ← stripe.left_endpoint
9: end ← stripe.right_endpoint
10: else
11: start ← stripe.right_endpoint
12: end ← stripe.left_endpoint
13: end if
14: G.append(Pose(start, orientation=direction))
15: G.append(Pose(end, orientation=direction))
16: direction ← direction × (-1)
17: end for
18: end for
19: return G

The `stripe_width` parameter is set to 0.25 m, slightly less than the roller brush width (0.28 m) to ensure overlap and eliminate uncovered gaps. The `DecomposeGrid` function uses a trapezoidal decomposition adapted from Choset [5], with a minimum cell area threshold of 0.25 m² to prevent over-segmentation.

2.4.3. State estimation and transform tree

The URDF/Xacro model defines the robot's physical properties (geometry, inertia, joints, sensors) and establishes a TF tree (map→odom→base_link→subframes) critical for SLAM, costmapping, and planning [22]. The navigation stack is modularly layered (perception, localization, planning, low-level control) [23], enabling planner swaps without firmware changes. Standard ROS 2 interfaces ensure parameter logging and cross-trial reproducibility, making the system both a functional cleaner and a flexible research testbed for autonomous coverage algorithms [24].

3. EXPERIMENTAL METHODOLOGY AND DESIGN

To rigorously validate the design and address concerns regarding experimental rigor, a comprehensive, controlled experimental methodology was established following ANSI/RIA R15.06 guidelines for robotic system evaluation. The study is explicitly framed as a controlled repeated-measures design incorporating both a treatment group (systematic Boustrophedon coverage) and a control group (random-walk navigation), enabling statistical comparison of performance metrics.

3.1. Experimental design and hypotheses

The primary objective is to verify design compliance and compare systematic versus stochastic navigation. The experiment employs a one-group pretest–posttest internal control design: treatment = autonomous Boustrophedon coverage with SLAM-based frontier exploration; control = random-walk with obstacle avoidance. Three hypotheses are tested ($\alpha = 0.05$): H_1 (Boustrophedon yields higher coverage efficiency), H_2 (Boustrophedon reduces path length per unit area), and H_3 (equivalence between measured pressure/deflection and CFD/FEA predictions).

3.2. Testing protocols

Suction performance testing. Static pressure rise was measured using a digital manometer (Testo 512, range 0–2000 Pa, accuracy ±0.5%) at the inlet and outlet of the dust filter. The suction motor was operated at its nominal voltage (12 V), and the flow rate was controlled by an adjustable orifice. Measurements were repeated 10 times for each condition; The reported values represent the mean ±

standard deviation. Fan efficiency was calculated from the measured static pressure rise ΔP, volumetric flow rate Q, and electrical input power P_{in} using:

$$\eta = \frac{\Delta P \cdot Q}{P_{\text{in}}}$$

Validation methodology. Mechanical integrity was assessed via three-point bending (ASTM D790) and quasi-static impact testing (20 N at 0.5 m/s) with strain-gauge monitoring at FEA-identified critical points. Thermal performance under full load (30 min) was recorded for all power components and the suction motor. Navigation was benchmarked over ten repeated runs in a 5×5 m standardized arena, measuring localization RMSE (via motion capture), area coverage, and collision counts. Generalizability was tested across a multi-room layout (35 m²), dynamic-obstacle trials (0.5 m/s pedestrian), and three floor surfaces. Sensor calibration encompassed LiDAR (known-distance scanning), IMU (six-position static method) [25], and wheel encoders (odometry vs. motion-capture ground truth over 10 m). Battery endurance was quantified over five repeated discharge cycles (12.6 V to 9.0 V cutoff) with all systems active.

3.3. Statistical analysis

All quantitative data are reported as mean ± standard deviation unless otherwise stated. Differences between the Boustrophedon treatment group and the random-walk control group were evaluated using paired-samples *t*-tests for navigation performance metrics (coverage efficiency, total path length, and collision count) and a one-way analysis of variance (ANOVA) to compare performance across diverse floor surfaces. Equivalence between numerical simulation results (CFD/FEA) and physical experimental measurements was assessed using two one-sided *t*-tests (TOST) with a predefined 10% equivalence margin. All statistical analyses were conducted in Python 3.11 using the SciPy 1.11 library. Effect sizes are reported as Cohen's *d* for *t*-tests and partial η^2 for ANOVA models.

4. RESULTS AND DISCUSSION

4.1. Suction and aerodynamic performance

The measured static pressure rise at the design flow rate was 198 ± 12 Pa (n = 10), showing close agreement with the CFD prediction of 210 Pa (relative deviation of 5.7%). Two one-sided equivalence testing (TOST) confirmed that the experimental measurements and numerical predictions are statistically equivalent within the predefined 10% equivalence bound ($t(18) = 2.14$, $p = 0.023$). The differential pressure drop across the dust filter was 18.2 ± 1.1 Pa, confirming that the developed impeller comfortably overcomes structural filtration resistance. Total fan efficiency—calculated from the measured static pressure rise ΔP, design volumetric flow rate (Q = 0.012 m³/s), and electrical power input—was 47.1%. This falls well within the characteristic 40%–50% efficiency range for miniature FDM-printed centrifugal impellers and slightly exceeds the baseline CFD prediction of 42% as a result of lower-than-expected parasitic shaft friction within the printed bearing housing.

4.2. Structural integrity

Under the 20 N impact load, the maximum measured displacement at the roller holder arm was 0.29 mm, demonstrating close agreement with the FEA prediction of 0.31 mm (relative error of 6.5%). Equivalence testing (TOST) confirmed that the physical measurements and simulation predictions exhibited no statistically significant deviation within the defined equivalence bounds ($t(18) = 1.89$, $p = 0.038$). Strain gauge readings across all monitored critical regions remained safely below the yield strain limit of the PLA+ material. Furthermore, no visible microcracking or permanent plastic deformation was observed following repeated impact cycles. The resulting factor of safety (FoS) of 4.8 under dynamic impact loading confirms that the additive-manufactured chassis possesses sufficient structural compliance to endure accidental collisions without catastrophic failure.

4.3. Thermal performance

After 30 minutes of continuous full-load operation, the peak temperatures recorded were: LM7805 regulators 62.3 °C, L298N driver 58. 7 °C, XL4016 converter 49.2 °C, and suction motor housing 58.1 °C. All remained below their respective derating limits (125 °C for LM7805, 150 °C for L298N, 85 °C for XL4016, and 80 °C for motor). The forced convection from the exhaust airflow contributed an estimated 8 °C reduction compared to a passive cooling scenario, validating the integrated thermal management strategy.

4.4. Navigation performance: controlled environment

Over the ten repeated runs in the 5 m × 5 m standardized environment, the average localisation RMSE was 0.042 m (standard deviation 0.011 m), demonstrating high accuracy for a low-cost platform. The average coverage efficiency was 97.3% (SD = 1.8%). The number of collisions per run averaged 2.1, primarily occurring at sharp corners. Map construction time for the 25 m² area averaged 47 seconds. CPU utilisation on the Raspberry Pi 4 averaged 62% across four cores, with peak usage during active SLAM loop closure (~85%). RAM occupancy was approximately 1.1 GB.

4.5. Comparative analysis: systematic vs. random-walk control

To validate the superiority of the systematic coverage strategy, Table 4 presents a direct comparison between the Boustrophedon treatment and the random-walk control under identical 5 m × 5 m test conditions. The random-walk algorithm was implemented by publishing forward velocity commands with random angular deflections upon obstacle detection, mimicking the behavior of entry-level commercial vacuums.

The Boustrophedon strategy achieved significantly higher coverage efficiency ($t(9) = 18.42$, $p < 0.001$, Cohen's $d = 2.41$), yielding a 34% reduction in path length required for complete coverage. In addition, physical collision frequency was reduced by 75% relative to the random-walk baseline control. These quantitative outcomes support hypotheses H1 and H2, validating that integrating SLAM-based systematic coverage path planning produces substantial, statistically significant enhancements in operational efficiency and navigation safety over stochastic exploration.

Table 4. Comparison of navigation strategies (Mean ± SD, n = 10 per group)

Platform	Cost (USD)	Suction Method	Navigation	Open Source?	Manufacturing
ZER0 (this work)	~308	Centrifugal, 198 Pa	LiDAR SLAM	✓	FDM
iRobot Create 3	1,300	N/A (dev platform)	Optional	SDK only	Injection
TurtleBot 4	~1,800	N/A	LiDAR SLAM	✓	Injection
Roomba 115	~290	Cyclone, generic	Random/Inertial	✗	Injection
Roborock Q7 M5+	~360	Cyclone, 10,000 Pa	LiDAR	✗	Injection

4.6. Extended scenario validation

Multi-room navigation. In the three-room, 35 m² layout, ZER0 successfully constructed a unified occupancy map and achieved a coverage efficiency of 94.8% (SD = 2.3%) across 10 trials. Doorway traversal success rate was 100%, although map merge latency increased to 78 s due to larger map size. Localisation RMSE remained stable at 0.048 m, indicating that the platform scales effectively to larger domestic layouts.Dynamic obstacles. When a human operator traversed the environment during cleaning, the DWB local planner successfully replanned trajectories in real time. Coverage efficiency dropped modestly to 93.1% (SD = 3.1%) as the robot paused to allow passage, but no collisions occurred. This demonstrates robustness to semi-static and dynamic interruptions typical of real households. A one-way ANOVA revealed no statistically significant difference in coverage efficiency across ceramic tile (97.3%), laminate wood (96.8%), and low-pile carpet (95.4%) ($F(2, 27) = 1.84$, $p = 0.18$, partial $\eta^2 = 0.12$). Although wheel slippage on carpet increased raw wheel-odometry drift by 12%, this was effectively compensated for by the LiDAR scan-matching and EKF fusion pipeline, successfully maintaining localization RMSE below 0.055 m across all evaluated surfaces.

4.7. Battery runtime

ZER0 achieved runtimes of 47.3 min (σ=2.1) and 44.8 min in multi-room scenarios, surpassing the 40-min target. Simulation predictions aligned with physical tests (errors <7%), validating its additive manufacturing approach. As an open-source system, it offers an integrated educational framework (CAD, aerodynamics, electronics, ROS 2), serves as a benchmark for future algorithms, and lowers entry barriers via released design files. Transferable design principles and a ~$308 cost (vs. 5–6x pricier alternatives) underscore its cost-effectiveness. Limitations include the controlled 5x5 m environment and absent long-term reliability data (e.g., cycling, filter wear), though multi-room trials suggest scalability; broader replication remains future work.

4.8. Cost analysis and platform comparison

The total bill-of-materials for ZER0 is approximately 308 USD. Including prototyping overhead, testing equipment, and consumables, the project cost is ~430 USD. Table 5 provides a consolidated BOM, while Table 6 contextualizes ZER0 against existing platforms, emphasizing that no alternative offers the

combination of integrated vacuuming, open-source hardware/software, SLAM navigation, and FDM manufacturing at comparable cost.

Table 5. Consolidated bill of materials

Category	Components	Cost ($)
Sensing & Logic	Raspberry Pi 4, RPLiDAR A1, IMU	142
Drive & Suction	775 Motor, GA25YN370 Motors, Encoders	24
Power & PCB	18650 Pack, XL4016, L298N, Custom PCB	142
Chassis & Misc	3D Printed PLA+ Components (~1.2kg), Hardware	22
Total	—	~308

Table 6. Comparison with existing platforms

Platform	Cost (USD)	Suction Method	Navigation	Open Source?	Manufacturing
ZER0 (this work)	~308	Centrifugal, 198 Pa	LiDAR SLAM	✓	FDM
iRobot Create 3	1,300	N/A (dev platform)	Optional	SDK only	Injection
TurtleBot 4	~1,800	N/A	LiDAR SLAM	✓	Injection
Roomba 115	~290	Cyclone, generic	Random/Inertial	✗	Injection
Roborock Q7 M5+	~360	Cyclone, 10,000 Pa	LiDAR	✗	Injection

The comparison underscores ZER0's unique positioning: it is the only platform that combines full vacuum functionality with open-source SLAM autonomy and additive manufacturing, at a cost comparable to entry-level proprietary vacuums.

4.9. Limitations and future work

The current iteration defines several paths for future development:

- Computational power: Transitioning from the Pi 4 to AI-dedicated hardware (e.g., NVIDIA Jetson) would enable object recognition and semantic mapping for more sophisticated environmental understanding.
- Energy density: The current 3S battery limits runtime to ~47 minutes at full load. Future work will involve autonomous docking stations and high-density LiPo energy storage with an integrated battery management system (BMS).
- Aerodynamic refinement: Topology optimization of the volute scroll and multi-stage impeller designs could increase pressure rise beyond the current 198 Pa, potentially exceeding 300 Pa while maintaining printability.
- Material evolution: Transitioning from FDM-printed PLA+ to injection-moulded components or carbon-fibre-reinforced polymers would improve structural consistency, surface finish, and long-term fatigue life.
- Sensor fusion: Integration of 3D LiDAR, RGB-D cameras, ultrasonic sensors, and cliff detection would enhance perception for complex, dynamic indoor environments.
- Long-term reliability: Extended lifecycle testing (500+ cleaning cycles) is required to characterize filter saturation dynamics, PLA+ creep under sustained load, and bearing wear in the printed impeller hub.

These limitations also define a clear pathway for reproducible follow-up studies. Longer-duration testing should be performed with repeated filter loading, repeated impeller operation, and multiple printed batches to quantify manufacturing variability. Cross-platform experiments could additionally isolate the contribution of the mechanical design from that of the navigation stack. Such studies would strengthen the evidence for generalizing the present results from a single prototype to a broader class of repairable, low-cost domestic service robots.

5. CONCLUSION

Experimental validation confirms ZER0 meets all design targets: PLA+ chassis (FOS > 4.8), centrifugal impeller delivering 198 Pa at 47.1% efficiency (matching CFD), electronics below 65 °C, and LiDAR-SLAM with Boustrophedon planning achieving 0.042 m RMSE and 97.3% coverage—significantly outperforming random-walk baselines—at ~$308 USD. Broader contributions include generalizable guidelines: hybrid chassis geometry, integrated exhaust-driven passive cooling, hierarchical galvanically isolated power distribution, and systematic planning for high coverage. The open-source release establishes a reproducible foundation for domestic automation, education, and sustainable, repairable consumer robotics.

FUNDING INFORMATION

Authors state no funding involved.

AUTHOR CONTRIBUTIONS STATEMENT

This journal uses the Contributor Roles Taxonomy (CRediT) to recognize individual author contributions, reduce authorship disputes, and facilitate collaboration.

Name of Author	C	M	So	Va	Fo	I	R	D	O	E	Vi	Su	P	Fu
Eman Ebrahim	✓	✓	✓	✓	✓	✓		✓	✓	✓			✓	
Ibrahim Al Souleiman		✓				✓		✓	✓	✓	✓	✓		

C : **C**onceptualization
M : **M**ethodology
So : **So**ftware
Va : **Va**lidation
Fo : **Fo**rmal analysis
I : **I**nvestigation
R : **R**esources
D : **D**ata Curation
O : Writing - **O**riginal Draft
E : Writing - Review & **E**diting
Vi : **Vi**sualization
Su : **Su**pervision
P : **P**roject administration
Fu : **Fu**nding acquisition

CONFLICT OF INTEREST STATEMENT

Authors state no conflict of interest.

DATA AVAILABILITY

The data that support the findings of this study, including the experimental measurements (static pressure, structural, thermal, navigation, and battery-runtime tests), the CFD/FEA simulation results, the CAD models, the PCB design files, and the ROS 2 source code of ZER0, are available from the corresponding author, E. E., upon reasonable request

REFERENCES

[1] M. Quigley *et al.*, "ROS: an open-source robot operating system," in *ICRA workshop on open source software*, 2009, vol. 3, no. 3.2, p. 5.
[2] J. D. Anderson, *Fundamentals of aerodynamics*. McGraw-Hill Education, 2017. [Online]. Available: https://books.google.co.id/books?id=_7VLjwEACAAJ
[3] I. Gibson, D. Rosen, B. Stucker, and M. Khorasani, *Additive manufacturing technologies*. Cham: Springer International Publishing, 2021. doi: 10.1007/978-3-030-56127-7.
[4] C. Cadena *et al.*, "Past, present, and future of simultaneous localization and mapping: toward the robust-perception age," *IEEE Transactions on Robotics*, vol. 32, no. 6, pp. 1309–1332, Dec. 2016, doi: 10.1109/TRO.2016.2624754.
[5] H. Choset, "Coverage for robotics – A survey of recent results," *Annals of Mathematics and Artificial Intelligence*, vol. 31, no. 1–4, pp. 113–126, Oct. 2001, doi: 10.1023/A:1016639210559.
[6] M. F. Ashby, *Materials selection in mechanical design*. Elsevier, 2011. doi: 10.1016/C2009-0-25539-5.
[7] Y. A. Çengel and J. M. Cimbala, *Fluid Mechanics: Fundamentals and Applications*. McGraw-Hill Education, 2018. [Online]. Available: https://books.google.co.id/books?id=DqFJvgAACAAJ
[8] Raspberry Pi Ltd, "Raspberry Pi 4 Model B," 2019. https://www.raspberrypi.com/products/raspberry-pi-4-model-b/
[9] SLAMTEC, "2D LiDAR Scanner -- RPLIDAR Series." [Online]. Available: https://www.slamtec.com
[10] STMicroelectronics, "L298N Dual Full-Bridge driver datasheet." [Online]. Available: https://www.st.com/resource/en/datasheet/l298.pdf
[11] XLSEMI, "XL4016E high efficiency DC-DC step down converter datasheet." [Online]. Available: http://www.xlsemi.com
[12] Texas Instruments, "LM7805 Series Voltage Regulators datasheet (SLVS057)." [Online]. Available: https://www.ti.com/lit/ds/symlink/lm7805.pdf
[13] Open Robotics, "Robot operating system (ROS) documentation." [Online]. Available: https://www.ros.org
[14] K. Konolige, "Small vision systems: Hardware and implementation," in *Robotics Research*, London: Springer London, 1998, pp. 203–212. doi: 10.1007/978-1-4471-1580-9_19.
[15] E. B. Olson, "Real-time correlative scan matching," in *2009 IEEE International Conference on Robotics and Automation*, May 2009, pp. 4387–4393. doi: 10.1109/ROBOT.2009.5152375.
[16] S. Macenski, F. Martín, R. White, and J. G. Clavero, "The Marathon 2: A navigation system," Jul. 2020. doi: 10.1109/IROS45743.2020.9341207.
[17] D. Fox, W. Burgard, and S. Thrun, "The dynamic window approach to collision avoidance," *IEEE Robotics & Automation Magazine*, vol. 4, no. 1, pp. 23–33, Mar. 1997, doi: 10.1109/100.580977.
[18] S. Thrun, W. Burgard, and D. Fox, *Probabilistic Robotics*. MIT Press, 2005. [Online]. Available: https://books.google.co.id/books?id=k_yOQgAACAAJ
[19] D. Fox, S. Thrun, W. Burgard, and F. Dellaert, "Particle filters for mobile robot localization," in *Sequential Monte Carlo Methods in Practice*, New York, NY: Springer New York, 2001, pp. 401–428. doi: 10.1007/978-1-4757-3437-9_19.
[20] W. Burgard, D. Fox, D. Hennig, and T. Schmidt, "Estimating the absolute position of a mobile robot using position probability grids," in *Proceedings of the national conference on artificial intelligence*, 1996, pp. 896–901.
[21] A. Elfes, "Using occupancy grids for mobile robot perception and navigation," *Computer*, vol. 22, no. 6, pp. 46–57, Jun. 1989,

doi: 10.1109/2.30720.
[22] G. Grisetti, C. Stachniss, and W. Burgard, "Improved techniques for grid mapping with Rao-Blackwellized particle filters," *IEEE Transactions on Robotics*, vol. 23, no. 1, pp. 34–46, Feb. 2007, doi: 10.1109/TRO.2006.889486.
[23] R. Siegwart, I. R. Nourbakhsh, and D. Scaramuzza, *Introduction to Autonomous Mobile Robots, second edition*. MIT Press, 2011. [Online]. Available: https://books.google.co.id/books?id=zys3AgAAQBAJ
[24] B. Siciliano and O. Khatib, "Robotics and the Handbook," 2016, pp. 1–6. doi: 10.1007/978-3-319-32552-1_1.
[25] InvenSense (TDK), "MPU-6050 Product Specification -- Six-Axis MEMS MotionTracking Device." [Online]. Available: https://invensense.tdk.com/products/motion-tracking/6-axis/mpu-6050/

BIOGRAPHIES OF AUTHORS



Eman Ebrahim is affiliated with Swiss International University (SIU) and conducts multidisciplinary engineering research spanning autonomous robotics, mechatronic system design, additive manufacturing, mechanical analysis, and experimental validation. In the present study, the author contributed to the mechanical architecture, FDM fabrication strategy, CFD/FEA validation, system integration, experimental methodology, and performance interpretation. Her research centers on developing accessible robotic platforms where mechanical design, embedded control, sensing, and autonomous navigation function as an integrated system. She can be contacted at dr.n.eman@swiss.edu.eu.



Ibrahim Al Souleiman is affiliated with Swiss International University (SIU) and contributes to research involving artificial intelligence, automation, digital systems, and interdisciplinary technology integration. In this study, the author contributed to the robotics software architecture, ROS 2 integration, navigation implementation, experimental validation, and manuscript revision. His work bridges physical mobile platforms with autonomous perception, localization, path planning, and control, emphasizing modular software architectures transferable to broader service-robot applications. He can be contacted at dr.i@swiss.edu.eu.